Available online at www.sciencedirect.com
SCIENCE DIRECT®
Journal of Computational Physics 194 (2004) 632–658
JOURNAL OF COMPUTATIONAL PHYSICS
www.elsevier.com/locate/jcp

Power ENO methods: a fifth-order accurate Weighted Power ENO method

Susana Serna [*,1], Antonio Marquina [1]

Applied Mathematics, University of Valencia, Dr. Moliner, 50 Burjassot 46100, Spain

Received 4 December 2002; received in revised form 24 September 2003; accepted 24 September 2003

Abstract

In this paper we introduce a new class of ENO reconstruction procedures, the Power ENO methods, to design high-order accurate shock capturing methods for hyperbolic conservation laws, based on an extended class of limiters, improving the behavior near discontinuities with respect to the classical ENO methods. Power ENO methods are defined as a correction of classical ENO methods [J. Comput. Phys. 71 (1987) 231], by applying the new limiters on second-order differences or higher. The new class of limiters includes as a particular case the minmod limiter and the harmonic limiter used for the design of the PHM methods [see SIAM J. Sci. Comput. 15 (1994) 892]. The main features of these new ENO methods are the substantially reduced smearing near discontinuities and the good resolution of corners and local extrema. We design a new fifth-order accurate Weighted Power ENO method that improves the behavior of Jiang–Shu WENO5 [J. Comput. Phys. 126 (1996) 202]. We present several one- and two-dimensional numerical experiments for scalar and systems of conservation laws, including linear advections and one- and two-dimensional Riemann problems for the Euler equations of gas dynamics, comparing our methods with the classical and weighted ENO methods, showing the advantages and disadvantages.

AMS: 65M06; 35L65; 76N15

Keywords: Conservation law; ENO; Weighted ENO; Total variation bounded

1. Introduction

In this paper, we shall consider numerical approximations to nonlinear conservation laws of the form:

$$\frac{\partial \mathbf{u}}{\partial t} + \sum_{i=1}^{d} \frac{\partial \mathbf{f}_i(\mathbf{u})}{\partial x_i} = 0, \tag{1}$$

* Corresponding author. Tel.: +34-96-354-4358.
E-mail addresses: susana.serna@uv.es (S. Serna), marquina@uv.es (A. Marquina).
[1] Research supported by DGICYT project BFM2001-2814.

0021-9991/$ - see front matter © 2003 Elsevier Inc. All rights reserved.
doi:10.1016/j.jcp.2003.09.017

where $\mathbf{u}$ is a m-dimensional vector of unknowns and $\mathbf{f}_i(\mathbf{u})$ are d vector-valued functions called *fluxes*. We assume strong hyperbolicity, i.e., the Jacobian matrices of the former system

$$\mathbf{A}_i = \frac{\partial \mathbf{f}_i(\mathbf{u})}{\partial \mathbf{u}} \tag{2}$$

locally diagonalize with real eigenvalues and a complete system of eigenvectors. The one-dimensional case of the system will be in the form

$$\mathbf{u}_t + (\mathbf{f}(\mathbf{u}))_x = 0, \tag{3}$$

with the initial value condition

$$\mathbf{u}(x,0) = \mathbf{u}_0(x). \tag{4}$$

Weak solutions of nonlinear conservation laws are piecewise smooth with jump discontinuities. High-order accurate numerical approximations to these functions are such that they achieve high accuracy on smooth regions and sharpen profiles of discontinuities, without spurious oscillations. Essentially non oscillatory (ENO), polynomial reconstruction procedures were designed to accomplish this purpose [4]. ENO methods are high-order accurate on smooth regions and appear to be very robust on shocks. However, several drawbacks became relevant after some experimentation with ENO methods took place, from which we mention:

1. Loss of accuracy on smooth regions with specific input data [14].
2. Smearing of certain discontinuities [5].
3. Smoothing up of corners. (discontinuities of the first derivative) [10].
4. Too wide stencil to get high-order accuracy [5].

In order to overcome those difficulties (see [14]), several remedies were proposed. Shu [17] proposed a more centered ENO selection to reduce the loss of accuracy. PHM methods were introduced to improve the resolution of corners. WENO methods were designed to get optimal accuracy for a specific stencil, degenerating to a classical ENO method at discontinuities.

In this paper we introduce a new class of parabolic ENO methods, we call the *Power ENO methods*, based on a class of limiters that contains *minmod* and ENO limiters as a particular case, as well as the limiters based on the harmonic mean, used to design the PHM methods and Harmonic ENO methods (see [1,7,10,11]). We focus our study on ENO parabolas and we apply the *limiters on neighboring second-order differences* in order to retain more information of fine scales. The main advantage of those methods with respect to the classical ENO methods is the improved behavior near discontinuities. In particular, we propose a new fifth-order accurate weighted ENO method with a better behavior near jumps and corners than the Jiang and Shu WENO5 described in [5]. A disadvantage of applying limiters on second-order differences is that there is a loss of accuracy near smooth inflection points.

The paper is organized as follows: In Section 2 we describe and discuss the new family of limiters. Section 3 is focused on our new Power ENO method, discussing the advantages and disadvantages, compared to the parabolic ENO method. In particular, we discuss the third-order accurate Power ENO3 method. In Section 4, we propose a new fifth-order accurate Weighted Power ENO method, designed as a convex combination of the three parabolas used to define the third-order accurate Power ENO method, following a similar procedure to the one used by Jiang and Shu [5]. In Section 5, we test our Power ENO and Weighted Power ENO methods on several one- and two-dimensional model problems, for scalar and systems of conservation laws, and we compare them with ENO3 and WENO5 schemes, to analyze their ability in resolving shocks and complex flow problems. Finally, we draw our conclusions in Section 6.

2. An extended class of limiters

The ENO, minmod and harmonic limiters were introduced to control the behavior of reconstructions around discontinuities, in order to avoid the Gibbs' phenomena and over/under-shoots. We want to get high-order accurate reconstruction methods without spurious oscillations near discontinuities. The limiters are usually based on a mean of two nonnegative numbers. Indeed,

$$\mathrm{minmod}(x,y) = \frac{(\mathrm{sign}(x)+\mathrm{sign}(y))}{2}\min(|x|,|y|), \tag{5}$$

$$\mathrm{mineno}(x,y) = \mathrm{minsign}(x,y)\min(|x|,|y|), \tag{6}$$

$$\mathrm{harmod}(x,y) = \frac{(\mathrm{sign}(x)+\mathrm{sign}(y))}{2}\frac{2|x||y|}{|x|+|y|}, \tag{7}$$

$$\mathrm{hareno}(x,y) = \mathrm{minsign}(x,y)\frac{2|x||y|}{|x|+|y|}, \tag{8}$$

where $\mathrm{sign}(x)$ is the sign function, and

$$\mathrm{minsign}(x,y) = \begin{cases} \mathrm{sign}(x); & |x| <= |y|, \\ \mathrm{sign}(y); & \text{otherwise.} \end{cases}$$

These limiters are based on the *min* and *harmonic* mean, respectively, between two nonnegative numbers.

We shall explore a wide class of averages, bounded above by the arithmetic mean, containing the harmonic mean and the minimum as particular cases. Indeed, if $x > 0$ and $y > 0$, then, for a natural number p, we define the power-p mean, $\mathrm{power}_p(x,y)$ as:

$$\mathrm{power}_p(x,y) = \frac{(x+y)}{2}\left(1-\left|\frac{x-y}{x+y}\right|^p\right). \tag{9}$$

The function $\mathrm{power}_p(x,y)$ is homogeneous of degree 1 as a function of two variables. It is easy to see that

$$\mathrm{power}_p(x,y) = \min(x,y)\left[1+\left|\frac{y-x}{y+x}\right|+\cdots+\left|\frac{y-x}{y+x}\right|^{p-1}\right]. \tag{10}$$

In particular, if $0 < x < y$ then

$$\mathrm{power}_p(x,y) = x\left[1+\left(\frac{y-x}{y+x}\right)+\cdots+\left(\frac{y-x}{y+x}\right)^{p-1}\right]. \tag{11}$$

This is a truncated geometric series with ratio $r = (y-x)/(y+x) > 0$ and $r < 1$.

The infinite series converges to $(x+y)/2$. Then, the following inequalities are satisfied for any $x > 0$ and $y > 0$:

$$\min(x,y) \leqslant \mathrm{power}_p(x,y) \leqslant \mathrm{power}_q(x,y) \leqslant \frac{x+y}{2}$$

for $0 < p < q$.

Moreover, for any $x > 0$ and $y > 0$, we have

$$\mathrm{power}_1(x,y) = \min(x,y), \tag{12}$$

$$\mathrm{power}_2(x,y) = \frac{2xy}{x+y}. \tag{13}$$

The above identities are very useful to compute the discrepancy between the arithmetic mean and the power-p means, in order to get simple expressions of the truncation errors, as we will see in the following section.

The following proposition describes a necessary condition for an average to be useful to design limiters in the reconstruction procedures that are piecewise smooth and its total variation in cells next to discontinuities is bounded. This property is not satisfied for the arithmetic mean, nor the geometric mean.

Proposition 1. *If $x(h) > 0$ and $y(h) > 0$ are functions of the real parameter $h > 0$, such that $x(h) = \mathrm{O}(1)$ and $y(h) = \mathrm{O}(1/h)$, then $\mathrm{power}_p(x(h), y(h)) = \mathrm{O}(1)$.*

This assertion follows easily from the identity (11).

Next, we discuss the above-defined means in order to know its scope, when used in the design of limiters. Thus, we can define the corresponding limiters:

$$\mathrm{powermod}_p(x,y) = \frac{(\mathrm{sign}(x) + \mathrm{sign}(y))}{2}\mathrm{power}_p(|x|,|y|), \tag{14}$$

$$\mathrm{powereno}_p(x,y) = \mathrm{minsign}(x,y)\mathrm{power}_p(|x|,|y|). \tag{15}$$

The following identities show that minmod, ENO and harmonic limiters are particular cases of the power-p limiters:

$$\mathrm{powermod}_1(x,y) = \mathrm{minmod}(x,y), \tag{16}$$

$$\mathrm{powereno}_1(x,y) = \mathrm{mineno}(x,y). \tag{17}$$

$$\mathrm{powermod}_2(x,y) = \mathrm{harmod}(x,y), \tag{18}$$

$$\mathrm{powereno}_2(x,y) = \mathrm{hareno}(x,y). \tag{19}$$

We use the example of a scalar conservation law to settle our notation and computational framework:

$$v_t + f(v)_x = 0, \tag{20}$$

$$v(x,t) = v_0(x), \tag{21}$$

where v_0 is a periodic or compactly supported piecewise smooth function.

We consider the following computational grid: $x_j = jh$ (h is the spatial step), $t_n = n\Delta t$, is the time discretization (Δt is the time step), $I_j = [x_{j-\frac{1}{2}}, x_{j+\frac{1}{2}}]$ is the spatial cell, where $x_{j+\frac{1}{2}} = x_j + \frac{h}{2}$ is the cell interface and $C_j^n = [x_{j-\frac{1}{2}}, x_{j+\frac{1}{2}}] \times [t_n, t_{n+1}]$ is the computational cell. Let v_j^n be an approximation of the mean value in I_j, $(1/h)\int_{x_{j-\frac{1}{2}}}^{x_{j+\frac{1}{2}}} v(x,t_n)\,\mathrm{d}x$, of the exact solution $v(x,t_n)$ of the initial value problem (20) and (21), obtained from a finite volume scheme in conservation form:

$$v_j^{n+1} = v_j^n - \frac{\Delta t}{h}(\tilde{f}_{j+\frac{1}{2}} - \tilde{f}_{j-\frac{1}{2}}), \tag{22}$$

where the numerical flux, $\tilde{f}$, is a function of $k+l$ variables

$$\tilde{f}_{j+\frac{1}{2}} = \tilde{f}(v^n_{j-k+1}, \ldots, v^n_{j+l}), \tag{23}$$

which is consistent with the flux of the Eq. (20),

$$\tilde{f}(v, \ldots, v) = f(v). \tag{24}$$

Following Harten [3], a consistent numerical scheme in conservation form (22) is TVD (total variation diminishing), if

$$\mathrm{TV}(v^{n+1}) \leqslant \mathrm{TV}(v^n), \tag{25}$$

where $\mathrm{TV}(v^n) = \sum_j |v^n_{j+1} - v^n_j|$ is the total variation of the discrete solution.

Next, we will analyze our limiters in terms of the classical flux limiter schemes which are TVD. We will focus our attention on the one-dimensional linear advection with constant wave speed $a > 0$:

$$v_t + a v_x = 0, \tag{26}$$

and, we consider a flux limiter scheme based on the Lax–Wendroff scheme applied to the above equation as the scheme in conservation form defined from the following numerical flux:

$$\tilde{f}_{j+\frac{1}{2}} = a v^n_j + \frac{a}{2}(1-\nu)(v^n_{j+1} - v^n_j)\phi_j, \tag{27}$$

where ϕ_j represents the flux limiter, i.e., it is a function $\phi_j = \phi(\theta_j)$, with

$$\theta_j = \frac{v^n_j - v^n_{j-1}}{v^n_{j+1} - v^n_j} \tag{28}$$

and $\nu = a(\Delta t/h)$. If $\phi(\theta)$ is bounded, $\phi(1) = 1$ and it is Lipschitz continuous at $\theta = 1$, then, the scheme is second-order accurate in space and time, except at local extrema where it degenerates to first order, (see [8,13]). For the sake of simplicity in our discussion on TVD property we assume that

$$\phi(\theta) = 0 \quad \text{if } \theta \leqslant 0. \tag{29}$$

From a theorem by Harten (see [3]) if a flux limiter function ϕ satisfies:

$$0 \leqslant \frac{\phi(\theta)}{\theta} \leqslant 2 \quad \text{and} \quad 0 \leqslant \phi(\theta) \leqslant 2 \qquad \text{for all } \theta, \tag{30}$$

then, the scheme (27) is TVD. If we define a flux limiter function from a limiter as

$$\phi^p(\theta) = \mathrm{powermod}_p(1, \theta), \tag{31}$$

we have that ϕ^p satisfies (29). The following lemma follows easily from the definition of the $\mathrm{powermod}_p$ limiters:

Proposition 2.

$$0 \leqslant \frac{\phi^p(\theta)}{\theta} \leqslant p \quad \textit{and} \quad 0 \leqslant \phi^p(\theta) \leqslant p \qquad \textit{for all } \theta.$$

Thus, for $p = 1, 2$, the ϕ^p function defines a TVD scheme, under the CFL restriction $|\nu| \leqslant 1$. On the other hand, for $p > 2$, it is not true that the flux limiter Lax–Wendroff scheme described above is TVD, under the

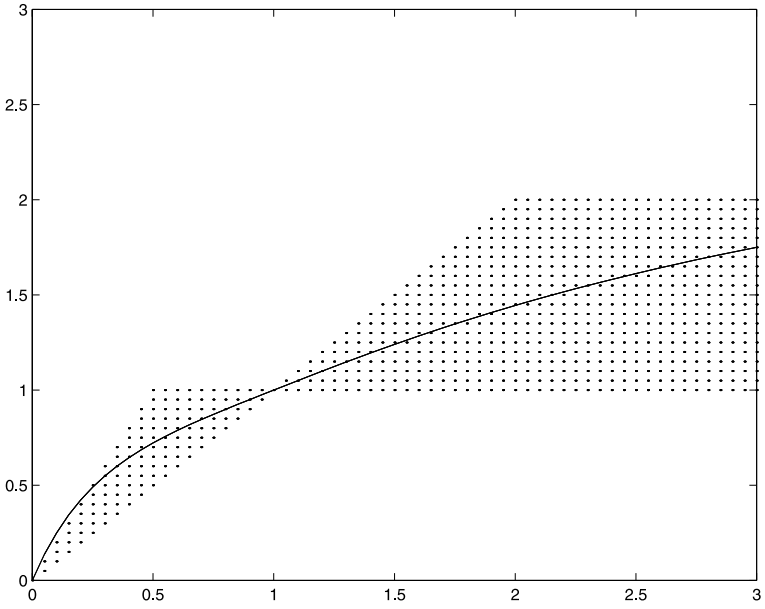

Fig. 1. TVD region and $\phi^3(\theta)$.

same CFL restriction (see Fig. 1). In fact, for $p = 3$, we have the restriction $\frac{1}{3} < |\nu| < \frac{2}{3}$, which is not useful. Thus, for $p > 2$ the powermod$_p$ and powereno$_p$ limiters should not be used for the schemes described above. This behavior can be observed in Fig. 1, where we represent $\phi^3(\theta)$ over the second-order TVD region (see [8] for details on TVD regions).

However, for methods of order of accuracy larger than two (and then, excluding Lax–Wendroff), second-order differences need to be limited like in ENO methods. When limiting second-order differences, small scales may be destroyed by using a very strong limiter like the one used for ENO methods. The "smearing effect" of ENO methods of order larger than 2 is, in part, due to the above reason. Here, we propose the powereno limiters for $p \geqslant 2$ to be applied to the second-order differences in order to retain (along the evolution) more information of fine scales.

In this paper we focus our study on the Power limiters for $p = 3$, based on the Power$_3$ mean, since it behaves essentially nonoscillatory near discontinuities (see Proposition 3), and it allows simple expressions of the local truncation errors when used as a limiter of second-order differences.

Formally, Power$_3$ mean can be written in the more convenient form:

$$\mathrm{Power}_3(x,y) = \min(x,y)\frac{x^2+y^2+2(\max(x,y))^2}{(x+y)^2}. \tag{32}$$

3. Piecewise polynomial reconstructions: Power ENO methods

We will use the notation introduced at the end of the above section.

For our purposes, a reconstruction procedure is an algorithm to obtain point values at the cell interfaces from cell averages and their differences corresponding to a set of discrete variables or fluxes, up to a degree of accuracy.

We want to reconstruct a function $u(x)$ from its mean values given at cells:

$$v_j = \frac{1}{h}\int_{x_{j-\frac{1}{2}}}^{x_{j+\frac{1}{2}}} u(x)\,\mathrm{d}x \tag{33}$$

such that u is a piecewise smooth function associated to the spatial grid defined above, i.e., u restricted to each cell I_j is smooth, and, therefore, possible jump discontinuities are located at cell interfaces. We denote by $r_j := u|I_j$, i.e., the restriction of u to I_j. Following (see [10, Definition 2.2, p. 897]), we say that a reconstruction procedure is *local total variation bounded* if $\mathrm{TV}(r_j) = \mathrm{O}(h)$, for all j, where TV denotes the total variation of the function r_j.

Our grid data are:

- (i) for every j the mean value of $u(x)$ in I_j, v_j is given to satisfy (33).
- (ii) for every j, $d_{j+\frac{1}{2}}$ is given by the undivided first-order difference:

$$d_{j+\frac{1}{2}} = v_{j+1} - v_j. \tag{34}$$

All the polynomial reconstruction methods analyzed in this paper have the same stencil as the classical ENO3 method and based on parabolas of the form:

$$p_j(x) = a_j + (x - x_j)\left[b_j + \frac{c_j}{2}(x - x_j)\right] \tag{35}$$

defined on I_j, where a_j, b_j and c_j are determinated from the grid data.

We use the following notations:

$$d_j = \frac{d_{j+\frac{1}{2}} + d_{j-\frac{1}{2}}}{2}, \tag{36}$$

$$D_j = d_{j+\frac{1}{2}} - d_{j-\frac{1}{2}}. \tag{37}$$

The classical ENO3 method is based on a selection procedure that chooses one parabola from three candidates:

$$p_{j-1}(x) = v_j - \frac{D_{j-1}}{24} + \frac{x - x_j}{h}\left[d_{j-\frac{1}{2}} + \frac{D_{j-1}}{2} + \frac{D_{j-1}}{2}\left(\frac{x - x_j}{h}\right)\right], \tag{38}$$

$$p_j(x) = v_j - \frac{D_j}{24} + \frac{x - x_j}{h}\left[d_j + \frac{D_j}{2}\left(\frac{x - x_j}{h}\right)\right], \tag{39}$$

$$p_{j+1}(x) = v_j - \frac{D_{j+1}}{24} + \frac{x - x_j}{h}\left[d_{j+\frac{1}{2}} - \frac{D_{j+1}}{2} + \frac{D_{j+1}}{2}\left(\frac{x - x_j}{h}\right)\right], \tag{40}$$

which correspond to the left-, central- and right-hand side choice, respectively. The ENO3 selection procedure to get the ENO parabola for the computational cell $C_j = [x_{j-\frac{1}{2}}, x_{j+\frac{1}{2}}]$ reads as follows:

if $|d_{j-\frac{1}{2}}| \leqslant |d_{j+\frac{1}{2}}|$ **then**
 if $|D_{j-1}| \leqslant |D_j|$ **then**
  $p_{j-1}(x)$
 else
  $p_j(x)$
 end

else
if $|D_j| \leqslant |D_{j+1}|$ **then**
$p_j(x)$
else
$p_{j+1}(x)$
end
end

To explore new ways to design ENO methods such that we get better behavior near discontinuities, we make to play in our study two new parabolas instead of the left and right choices used in ENO3. We construct these new parabolas using an intermediate value between two neighboring second-order differences:

$$p^M_{j-\frac{1}{2}}(x) = v_j - \frac{M_{j-\frac{1}{2}}}{24} + \frac{x-x_j}{h}\left[d_{j-\frac{1}{2}} + \frac{M_{j-\frac{1}{2}}}{2} + \frac{M_{j-\frac{1}{2}}}{2}\left(\frac{x-x_j}{h}\right)\right], \tag{41}$$

$$p^M_{j+\frac{1}{2}}(x) = v_j - \frac{M_{j+\frac{1}{2}}}{24} + \frac{x-x_j}{h}\left[d_{j+\frac{1}{2}} - \frac{M_{j+\frac{1}{2}}}{2} + \frac{M_{j+\frac{1}{2}}}{2}\left(\frac{x-x_j}{h}\right)\right], \tag{42}$$

where $M_{j-\frac{1}{2}} := \mathrm{mean}(D_{j-1}, D_j)$ and $M_{j+\frac{1}{2}} := \mathrm{mean}(D_j, D_{j+1})$, where "mean" is an intermediate value that eventually may be a limiter.

Next, we introduce the third-order accurate *Power ENO* method. We will use the $\mathrm{powereno}_3$ or $\mathrm{powermod}_3$ limiters (the limiters based on the mean power_3), computed at two neighboring second-order differences, at the place of the mean M, mentioned above. For the sake of simplicity, we refer to those limiters as *powereno* and *powermod* avoiding the subindex.

We will use the following three parabolas:

$$p^P_{j-\frac{1}{2}}(x) = v_j - \frac{P_{j-\frac{1}{2}}}{24} + \frac{x-x_j}{h}\left[d_{j-\frac{1}{2}} + \frac{P_{j-\frac{1}{2}}}{2} + \frac{P_{j-\frac{1}{2}}}{2}\left(\frac{x-x_j}{h}\right)\right], \tag{43}$$

$$p_j(x) = v_j - \frac{D_j}{24} + \frac{x-x_j}{h}\left[d_j + \frac{D_j}{2}\left(\frac{x-x_j}{h}\right)\right], \tag{44}$$

$$p^P_{j+\frac{1}{2}}(x) = v_j - \frac{P_{j+\frac{1}{2}}}{24} + \frac{x-x_j}{h}\left[d_{j+\frac{1}{2}} - \frac{P_{j+\frac{1}{2}}}{2} + \frac{P_{j+\frac{1}{2}}}{2}\left(\frac{x-x_j}{h}\right)\right], \tag{45}$$

which correspond to the left-, central- and right-hand side choice, respectively and $P_{j-\frac{1}{2}} = \mathrm{powereno}(D_{j-1}, D_j)$ and $P_{j+\frac{1}{2}} = \mathrm{powereno}(D_j, D_{j+1})$. Powermod limiter might be used instead, being less oscillatory, but we did not find significant computational differences.

Then, the Power-ENO3 method is defined choosing one of the above parabolas following the selection procedure of the classical ENO3 method. If we use the $\mathrm{powereno}_1$ limiter instead of powereno, we recover the ENO3 method.

In [10], it was shown that ENO3 method is local total variation bounded. Following analogous argument it is easy to show that:

Proposition 3. *The Power ENO3 method is local total variation bounded, i.e.,* $\mathrm{TV}(r) = \mathrm{O}(h)$*, where* r_j *is the reconstruction for the cell* C_j *and* h *is the spatial step.*

4. A fifth-order accurate Weighted Power ENO method

In order to show the prospective interest of our Power ENO method, we shall construct a new weighted ENO method as a convex combination of the three parabolas (43)–(45) used for our Power-ENO3 method. Then, in order to compute the optimal linear weights for this method we need to know simple expressions of the truncation errors for the above mentioned parabolas. We can obtain simple expressions using the arithmetic mean, instead of our nonlinear limiter.

Proposition 4. *If we use the arithmetic mean A, i.e.,* $A(x,y) := \frac{x+y}{2}$*, for the parabolas* (41) *and* (42)*, then, we have the following truncation error expressions at the right interface,* $x_{j+\frac{1}{2}}$*:*

$$p^A_{j-\frac{1}{2}}(x_{j+\frac{1}{2}}) - u = -4\left(\frac{h}{2}\right)^3 \frac{u'''}{6} + \frac{256}{5}\left(\frac{h}{2}\right)^4 \frac{u^{(\mathrm{iv})}}{24} + \mathrm{O}(h^5), \tag{46}$$

$$p^A_{j+\frac{1}{2}}(x_{j+\frac{1}{2}}) - u = -\frac{64}{5}\left(\frac{h}{2}\right)^4 \frac{u^{(\mathrm{iv})}}{24} + \mathrm{O}(h^6). \tag{47}$$

Proof. The Taylor expansion of $u(x)$ is

$$u(x) = u(x_j) + u'(x_j)(x-x_j) + u''(x_j)\frac{(x-x_j)^2}{2} + u'''(x_j)\frac{(x-x_j)^3}{6} + u^{(\mathrm{iv})}(x_j)\frac{(x-x_j)^4}{24} + \mathrm{O}(h^5).$$

Then, by computing (33) we get the Taylor expansions of the cell averages:

$$v_j = u(x_j) + \frac{1}{6}\left(\frac{h}{2}\right)^2 u''(x_j) + \frac{1}{120}\left(\frac{h}{2}\right)^4 u^{(\mathrm{iv})}(x_j) + \mathrm{O}(h^6). \tag{48}$$

We want to obtain the Taylor expansions, located at the right interface $x_{j+\frac{1}{2}}$, thus, for simplicity we denote by u, u', u'', u''', $u^{(\mathrm{iv})}$, $u^{(\mathrm{v})}$, the values of those functions evaluated at $x_{j+\frac{1}{2}}$.

$$u(x_j) = u - \frac{h}{2}u' + \left(\frac{h}{2}\right)^2\frac{u''}{2} - \left(\frac{h}{2}\right)^3\frac{u'''}{6} + \left(\frac{h}{2}\right)^4\frac{u^{(\mathrm{iv})}}{24} + \mathrm{O}(h^5),$$

$$u''(x_j) = u'' - \frac{h}{2}u''' + \left(\frac{h}{2}\right)^2\frac{u^{(\mathrm{iv})}}{2} + \mathrm{O}(h^3),$$

$$u^{(\mathrm{iv})}(x_j) = u^{(\mathrm{iv})} - \frac{h}{2}u^{(\mathrm{v})} + \mathrm{O}(h^2).$$

Therefore, the Taylor expansion of v_j at $x_{j+\frac{1}{2}}$ will be

$$v_j = u - \frac{h}{2}u' + \frac{4}{3}\left(\frac{h}{2}\right)^2\frac{u''}{2} - 2\left(\frac{h}{2}\right)^3\frac{u'''}{6} + \frac{16}{5}\left(\frac{h}{2}\right)^4\frac{u^{(\mathrm{iv})}}{24} + \mathrm{O}(h^5). \tag{49}$$

The corresponding expressions for $v_{j+1}, v_{j-1}, v_{j+2}$ and v_{j-2}, are obtained in a similar way and read as follows:

$$v_{j+1} = u + \frac{h}{2}u' + \frac{4}{3}\left(\frac{h}{2}\right)^2\frac{u''}{2} + 2\left(\frac{h}{2}\right)^3\frac{u'''}{6} + \frac{16}{5}\left(\frac{h}{2}\right)^4\frac{u^{(\mathrm{iv})}}{24} + \mathrm{O}(h^5),$$

$$v_{j-1} = u - 3\frac{h}{2}u' + \frac{28}{3}\left(\frac{h}{2}\right)^2\frac{u''}{2} - 30\left(\frac{h}{2}\right)^3\frac{u'''}{6} + \frac{496}{5}\left(\frac{h}{2}\right)^4\frac{u^{(\mathrm{iv})}}{24} + \mathrm{O}(h^5),$$

$$v_{j+2} = u + 3\frac{h}{2}u' + \frac{28}{3}\left(\frac{h}{2}\right)^2\frac{u''}{2} + 30\left(\frac{h}{2}\right)^3\frac{u'''}{6} + \frac{496}{5}\left(\frac{h}{2}\right)^4\frac{u^{(\mathrm{iv})}}{24} + \mathrm{O}(h^5),$$

$$v_{j-2} = u - 5\frac{h}{2}u' + \frac{76}{3}\left(\frac{h}{2}\right)^2\frac{u''}{2} - 130\left(\frac{h}{2}\right)^3\frac{u'''}{6} + \frac{3376}{5}\left(\frac{h}{2}\right)^4\frac{u^{(\mathrm{iv})}}{24} + \mathrm{O}(h^5).$$

Thus, after a straightforward computation, we obtain

$$p^A_{j+\frac{1}{2}}(x_{j+\frac{1}{2}}) = u - \frac{64}{5}\left(\frac{h}{2}\right)^4\frac{u^{(\mathrm{iv})}}{24} + \mathrm{O}(h^6), \tag{50}$$

i.e., $p_{j+\frac{1}{2}}$ is fourth-order accurate at $x_{j+\frac{1}{2}}$, and

$$p^A_{j-\frac{1}{2}}(x_{j+\frac{1}{2}}) = u - 4\left(\frac{h}{2}\right)^3\frac{u'''}{6} + \frac{256}{5}\left(\frac{h}{2}\right)^4\frac{u^{(\mathrm{iv})}}{24} + \mathrm{O}(h^5). \tag{51}$$

We need to use other limiters, at the place of the arithmetic mean, to get total variation stable reconstructions, in a way that, the truncation error expressions above are valid up to the highest possible order.

We apply our limiters on neighboring second-order central differences. Thus, if x and y are neighboring second-order central differences computed on a smooth region, we have that $x = \mathrm{O}(h^2)$, $y = \mathrm{O}(h^2)$ and $x - y = \mathrm{O}(h^3)$ and, therefore,

Proposition 5.

$$\frac{x+y}{2} - \mathrm{power}_p(x,y) = \mathrm{O}(h^{p+2}).$$

Proof. It follows easily from

$$\frac{x+y}{2} - \mathrm{power}_p(x,y) = \frac{x+y}{2}\left[1 - 1 + \left|\frac{x-y}{x+y}\right|^p\right] = \frac{x+y}{2}\left|\frac{x-y}{x+y}\right|^p = \mathrm{O}(h^{2+p}). \tag{52}$$

Thus, the next theorem follows from Proposition 5.

Theorem 1. *The following statements are true:*

1. *The truncation error expressions of the arithmetic mean are valid up to third-order terms for the* harmod *and* hareno *limiters* (*the power$_p$ limiters with $p = 2$*).
2. *The truncation error expressions of the arithmetic mean are valid up to fourth-order terms for the powermod and powereno limiters.*

From Proposition 4 and Theorem 1, the following truncation error expressions at the right interface are valid:

$$p^P_{j-\frac{1}{2}}(x_{j+\frac{1}{2}}) - u = -4\left(\frac{h}{2}\right)^3 \frac{u'''}{6} + \frac{256}{5}\left(\frac{h}{2}\right)^4 \frac{u^{(\mathrm{iv})}}{24} + \mathrm{O}(h^5),$$

$$p_j(x_{j+\frac{1}{2}}) - u = 4\left(\frac{h}{2}\right)^3 \frac{u'''}{6} - \frac{64}{5}\left(\frac{h}{2}\right)^4 \frac{u^{(\mathrm{iv})}}{24} + \mathrm{O}(h^5),$$

$$p^P_{j+\frac{1}{2}}(x_{j+\frac{1}{2}}) - u = -\frac{64}{5}\left(\frac{h}{2}\right)^4 \frac{u^{(\mathrm{iv})}}{24} + \mathrm{O}(h^6).$$

Thus, from the above expressions we can reach fifth-order accuracy at smooth regions, obtaining the optimal degree of accuracy, using an analogous procedure to the one used in [5] (see also [9]).

Indeed, in this case the optimal linear weights C_k to get this accuracy are uniquely defined, at the right interface, as the convex combination:

$$w_0 \cdot p^P_{j-\frac{1}{2}}(x_{j+\frac{1}{2}}) + w_1 \cdot p_j(x_{j+\frac{1}{2}}) + w_2 \cdot p^P_{j+\frac{1}{2}}(x_{j+\frac{1}{2}}), \tag{53}$$

where

$$w_k = \frac{\alpha_k}{\alpha_0 + \alpha_1 + \alpha_2} \tag{54}$$

for $k = 0, 1, 2$, and

$$\alpha_k = \frac{C_k}{(\epsilon + \mathrm{IS}_k)^2}, \tag{55}$$

where $C_0 = 0.2$, $C_1 = 0.2$ and $C_2 = 0.6$ are the optimal weights (we remind that the corresponding linear optimal weights for the WENO5 method are $C_0 = 0.1$, $C_1 = 0.3$ and $C_2 = 0.6$, see [5]).

Now, we use the L^2-norm of the derivatives of the polynomials involved (formula originally proposed by Jiang and Shu, see [5]), to get the smoothness indicators, that reach the optimal degree of accuracy, for this case. We obtain the following expressions:

$$\mathrm{IS}_0 = \frac{13}{12}\left(P_{j-\frac{1}{2}}\right)^2 + \frac{1}{4}\left(2v_j - 2v_{j-1} + P_{j-\frac{1}{2}}\right)^2, \tag{56}$$

$$\mathrm{IS}_1 = \frac{13}{12}\left(v_{j-1} - 2v_j + v_{j+1}\right)^2 + \frac{1}{4}\left(v_{j-1} - v_{j+1}\right)^2, \tag{57}$$

$$\mathrm{IS}_2 = \frac{13}{12}\left(P_{j+\frac{1}{2}}\right)^2 + \frac{1}{4}\left(2v_{j+1} - 2v_j - P_{j+\frac{1}{2}}\right)^2, \tag{58}$$

where P is the *powereno* or *powermod* limiter, computed for the two neighboring second-order differences.

Thus, the resulting method is a fifth-order accurate Weighted Power ENO method, we will call Weighted Power-ENO5.

We can compare with the indicators obtained for the Jiang–Shu WENO5 method (see [5]):

$$\mathrm{IS}_{0_{\mathrm{WENO5}}} = \tfrac{13}{12}\left(v_{j-2} - 2v_{j-1} + v_j\right)^2 + \tfrac{1}{4}\left(v_{j-2} - 4v_{j-1} + 3v_j\right)^2,$$

$$\mathrm{IS}_{1_{\mathrm{WENO5}}} = \tfrac{13}{12}\left(v_{j-1} - 2v_j + v_{j+1}\right)^2 + \tfrac{1}{4}\left(v_{j-1} - v_{j+1}\right)^2,$$

$$\mathrm{IS}_{2_{\mathrm{WENO5}}} = \tfrac{13}{12}\left(v_j - 2v_{j+1} + v_{j+2}\right)^2 + \tfrac{1}{4}\left(3v_j - 4v_{j+1} + v_{j+2}\right)^2,$$

and we remark that the central one is exactly the same.

The Taylor expansions of (56)–(58) in smooth regions are:

$$\mathrm{IS}_0 = \tfrac{13}{12}\left(u''h^2\right)^2 + \tfrac{1}{4}(2u'h - u''h^2 + \tfrac{1}{6}u'''h^3)^2 + \mathrm{O}(h^6),$$

$$\mathrm{IS}_1 = \tfrac{13}{12}\left(u''h^2\right)^2 + \tfrac{1}{4}(2u'h + \tfrac{1}{3}u'''h^3)^2 + \mathrm{O}(h^6),$$

$$\mathrm{IS}_2 = \tfrac{13}{12}\left(u''h^2\right)^2 + \tfrac{1}{4}(2u'h - u''h^2 + \tfrac{1}{6}u'''h^3)^2 + \mathrm{O}(h^6),$$

and, therefore, we have the same advantages than the ones obtained for the Jiang–Shu WENO5 method.

We compare the behavior of the smoothness measurement for our Weighted Power-ENO5 and the Jiang–Shu WENO5 in smooth regions and near critical points (jump discontinuities, discontinuities in derivative, etc.). First, we compute the weights w_0, w_1 and w_2 for the following function (proposed by Jiang and Shu [5]), at all right interfaces $x_{j+\frac{1}{2}}$, $x_j = jh$, $h = \frac{1}{40}$

$$u(x,0) = \begin{cases} \sin 2\pi x, & 0 \leqslant x \leqslant 0.5, \\ 1 - \sin 2\pi x, & 0.5 < x \leqslant 1. \end{cases}$$

We display the weights w_1 and w_2 in Fig. 2 for both methods. We observe that for the smooth region, both measurements behave similarly, that is, they achieve the optimal weights for fifth-order accuracy. Both methods degenerate to the corresponding digital ENO method (ENO3 or Power ENO3) at the points of discontinuity. However, at the points next to the discontinuity, our method get optimal weights of accuracy and the WENO5 weights degenerates to third-order accuracy.

Secondly, we compute the weights w_0, w_1 and w_2 for the function, u, defined on $[-1,1]$, with two discontinuities in the first derivative, at all right interfaces $x_{j+\frac{1}{2}}$, with $x_j = -1 + jh$ and $h = \frac{1}{40}$:

$$u(x,0) = \begin{cases} \sin\left(\pi \frac{x+0.6}{1.2}\right), & -0.6 \leqslant x \leqslant 0.6, \\ 0, & \text{otherwise.} \end{cases}$$

We display the weights w_1 and w_2 in Fig. 3 for both methods. We observe that our method only degenerates to the digital Power ENO3 at one point to resolve each critical point, while WENO5 degenerates to third order at two points next to each critical point.

Next, we focus our attention on testing the accuracy of our Weighted Power-ENO5 method on the linear advection initial value problem:

$$u_t + u_x = 0, \tag{59}$$

$$u(x,0) = \tfrac{1}{2}\left(\tfrac{1}{2} + \sin(2\pi x)\right). \tag{60}$$

We have implemented a third-order Runge–Kutta method [18] integration in time using a time step $\Delta t \approx (\Delta x)^{5/3}$ so that we reach fifth-order accuracy in time.

The use of nonsmooth limiters as, in our case, the powereno limiter, makes the numerical convergence noisier. The nonsmooth behavior of powereno limiter follows easily from (32) written in terms of the max and min functions. From the Taylor expansions discussed above it follows that when the second-order differences does not change sign the powereno is enough smooth to reach optimal accuracy, but at the smooth inflection points, the lack of regularity of the limiter makes our scheme less accurate.

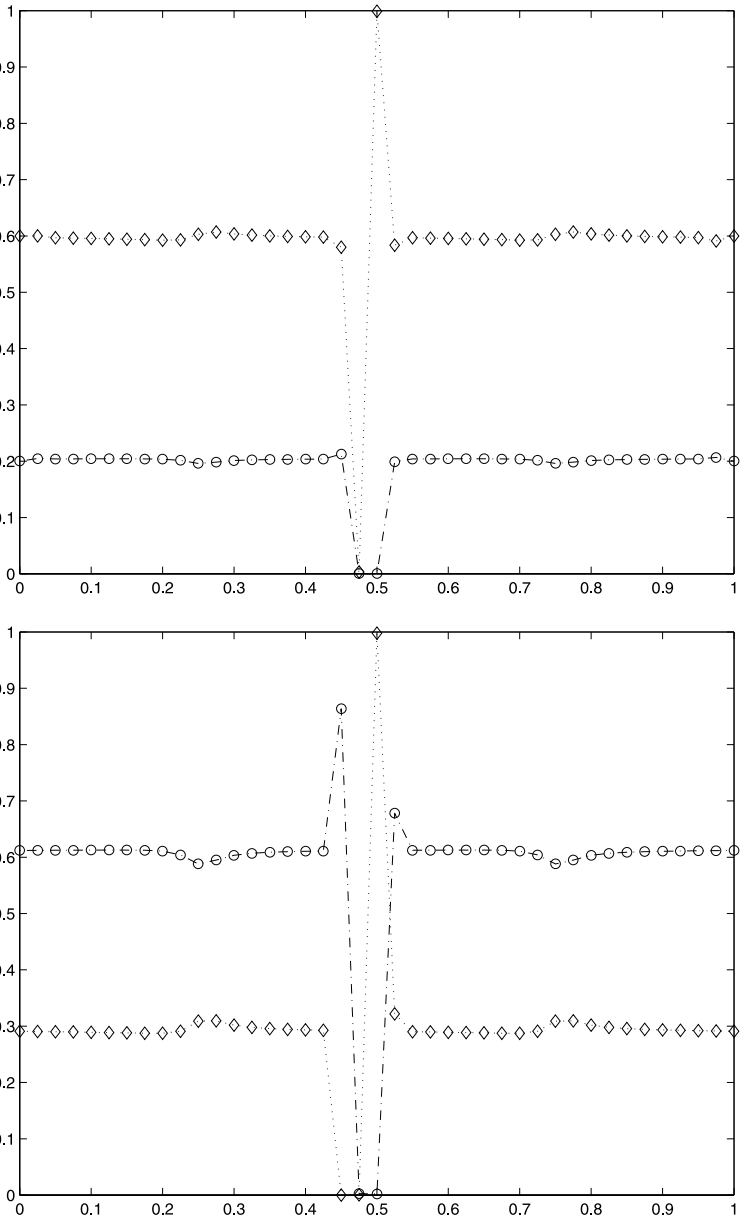

Fig. 2. A comparison of smoothness measurements for a jump discontinuity: Weighted Power-ENO5 (top) and WENO5 (bottom).

We display in Tables 1 and 2 the L_1 and L_∞ absolute errors and numerical orders, respectively, computed for both methods. We observe for the Weighted Power ENO method that there is a loss of accuracy (still present when refining the grid), as it can be seen at the table of absolute errors. This is due to numerical degeneration occurring near inflection points.

In order to check numerically this claim we display in Table 3, the corresponding L_1 and L_∞ errors removing a small neighborhood of the inflection points for different grids. We obtain in this case similar $L_1$and L_∞ errors to the corresponding values for the Jiang–Shu WENO5 method.

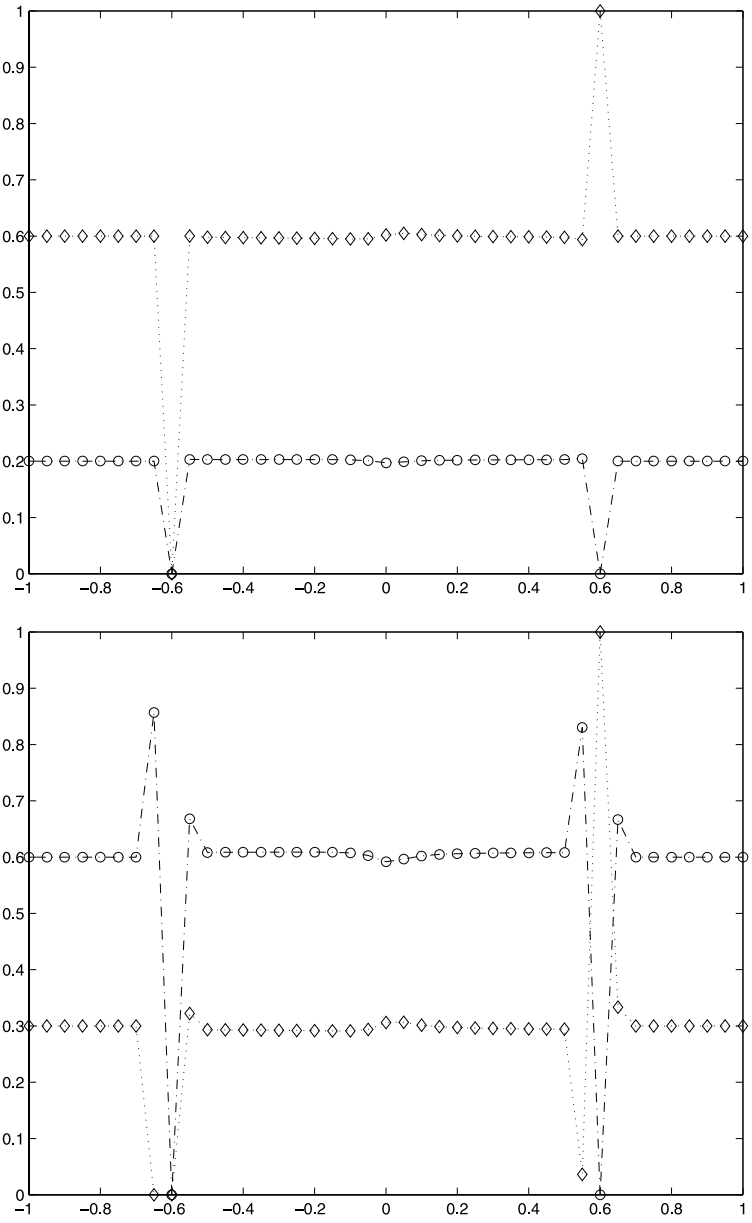

Fig. 3. A comparison of smoothness measurements for two discontinuities in derivative: Weighted Power-ENO5 (top) and WENO5 (bottom).

5. Numerical experiments

We start our calculations with the linear advection of signals. We will consider the following problems:

Table 1
Absolute errors for Weighted Power ENO5 and WENO5 methods

N	L_1-error		L_∞-error	
	Weighted Power-ENO5	WENO5	WPower-ENO5	WENO5
80	1.75×10^{-5}	7.17×10^{-7}	1.53×10^{-4}	1.37×10^{-6}
160	9.40×10^{-7}	2.24×10^{-8}	9.58×10^{-6}	4.18×10^{-8}
320	3.09×10^{-8}	7.08×10^{-10}	6.27×10^{-7}	1.23×10^{-9}
640	1.40×10^{-9}	2.29×10^{-11}	6.86×10^{-8}	4.02×10^{-11}
1280	5.01×10^{-11}	7.03×10^{-13}	2.67×10^{-9}	1.06×10^{-12}

Table 2
Numerical orders for Weighted Power-ENO5 and WENO5 methods

N	L_1-order		L_∞-order	
	WPower-ENO5	WENO5	WPower-ENO5	WENO5
160	–	–	–	–
320	4.22	4.99	3.86	5.04
640	4.97	4.99	4.46	5.08
1280	4.80	5.01	4.68	5.04

Table 3
Absolute errors for Weighted Power ENO5 and WENO5, excluding inflection points

N	L_1-error		L_∞-error	
	WPower-ENO5	WENO5	WPower-ENO5	WENO5
80	4.17×10^{-6}	8.76×10^{-7}	1.62×10^{-5}	1.35×10^{-6}
160	9.85×10^{-8}	2.72×10^{-8}	6.88×10^{-7}	4.18×10^{-8}
320	2.00×10^{-10}	8.27×10^{-10}	9.84×10^{-10}	1.23×10^{-9}
640	6.89×10^{-12}	2.46×10^{-11}	4.81×10^{-11}	4.01×10^{-11}

5.1. Example 1: Linear advection

We solve the linear equation

$$u_t + u_x = 0, \quad a \leqslant x \leqslant b,$$

with $u(x,0) = u_0(x)$ periodic in $[a,b]$, for the cases:

5.1.1. Example 1.1

$[a,b] = [0,1]$ and

$$u_0(x) = \begin{cases} 1, & 0.35 \leqslant x \leqslant 0.65, \\ 0, & \text{otherwise.} \end{cases}$$

5.1.2. Example 1.2

$[a,b] = [-1,1]$ and

$$u_0(x) = \begin{cases} \sin\left(\pi \frac{x+0.3}{0.6}\right), & -0.3 \leqslant x \leqslant 0.3, \\ 0, & \text{otherwise.} \end{cases}$$

All the calculations were performed using the upwind method and the Shu–Osher third-order Runge–Kutta integration in time (see [18]), with a grid of 100 points, $\Delta t/h = 0.5$, and total time of two periods.

In Fig. 4, we display the numerical approximation of Section 5.1.1 using the ENO3 and Power-ENO3 methods represented with '+' and 'o' signs, respectively. We observe an improved behavior near discontinuities for our Power-ENO3 method. The same calculations were done for Section 5.1.2, and we observe in Fig. 5 better resolution of corners for our Power-ENO3 method.

The above experiments show that the influence of the end points of the stencil is weaker for our PowerENO3 method thanks to the effect of the limiter.

In Fig. 6, we display the numerical approximation of Section 5.1.1 using WENO5 and WPower-ENO5 methods represented with '+' and 'o' signs, respectively. We observe the better behavior of our WPower-ENO5 near discontinuities. The same calculation was done for the Section 5.1.2 using both fifth-order accurate reconstruction procedures as displayed in Fig. 7. Here, the better behavior is justified since two reasons, namely: the narrower band of degeneration of accuracy for our method (see Figs. 2 and 3), and the better behavior near discontinuities inherited from the same feature observed for our PowerENO3 method.

Next, we perform numerical tests with Euler equations of gas dynamics. Let us consider first the one-dimensional Euler equations of gas dynamics

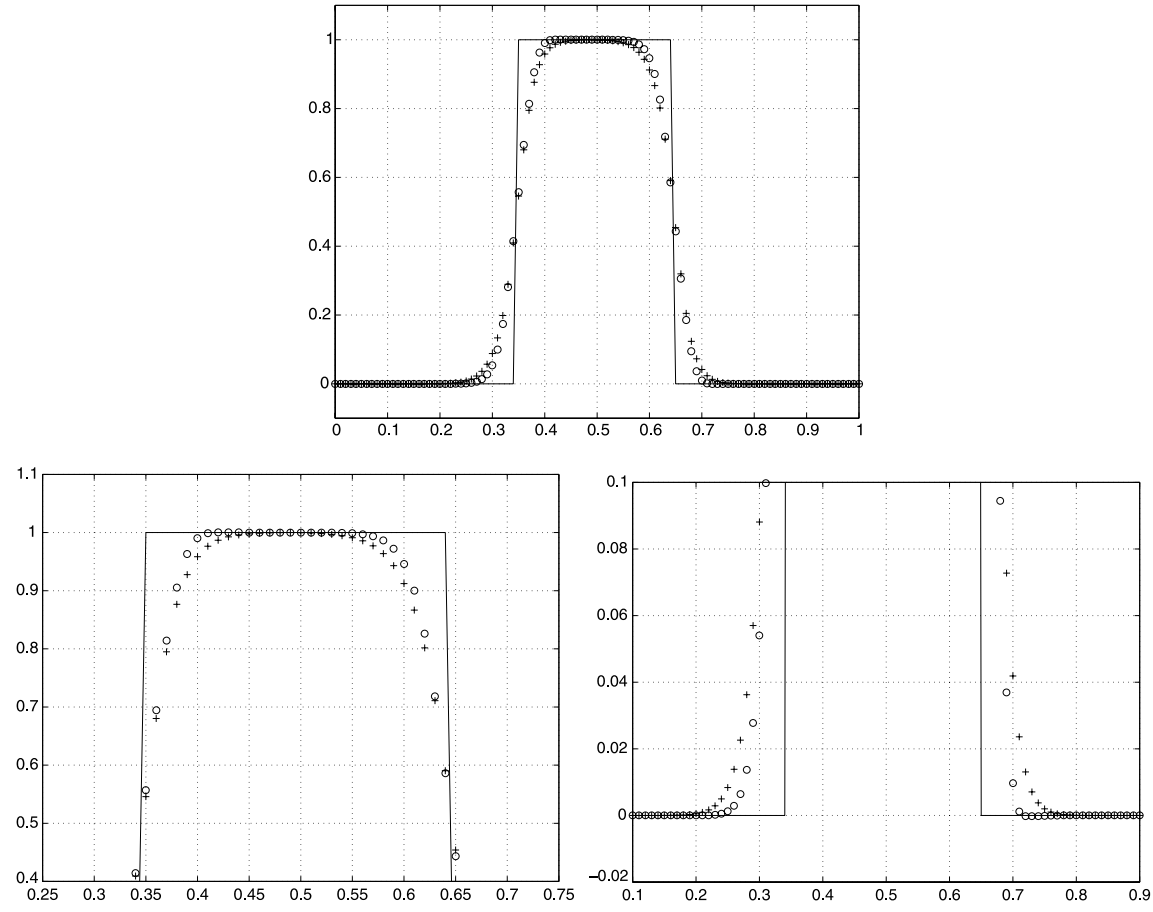

Fig. 4. ENO3 "+" and PowerENO3 "o".

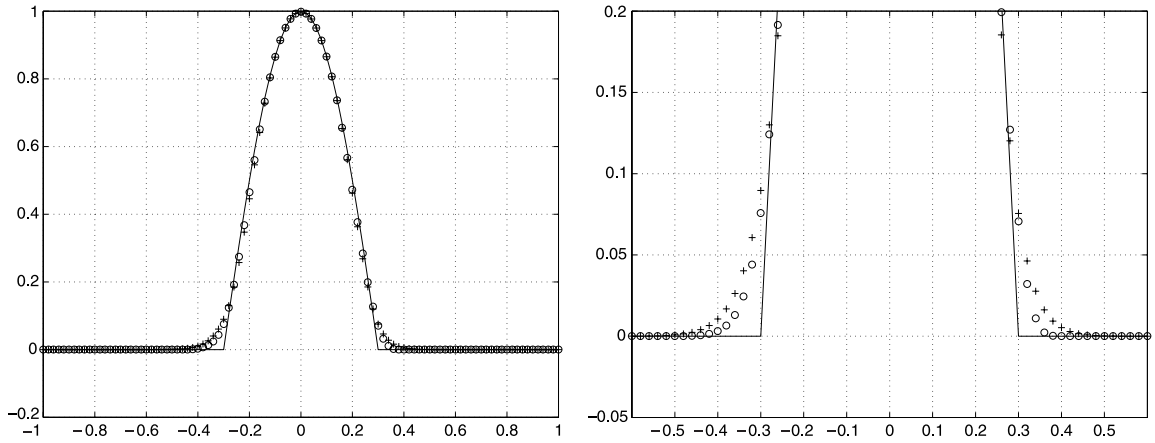

Fig. 5. ENO3 "+" and PowerENO3 "o".

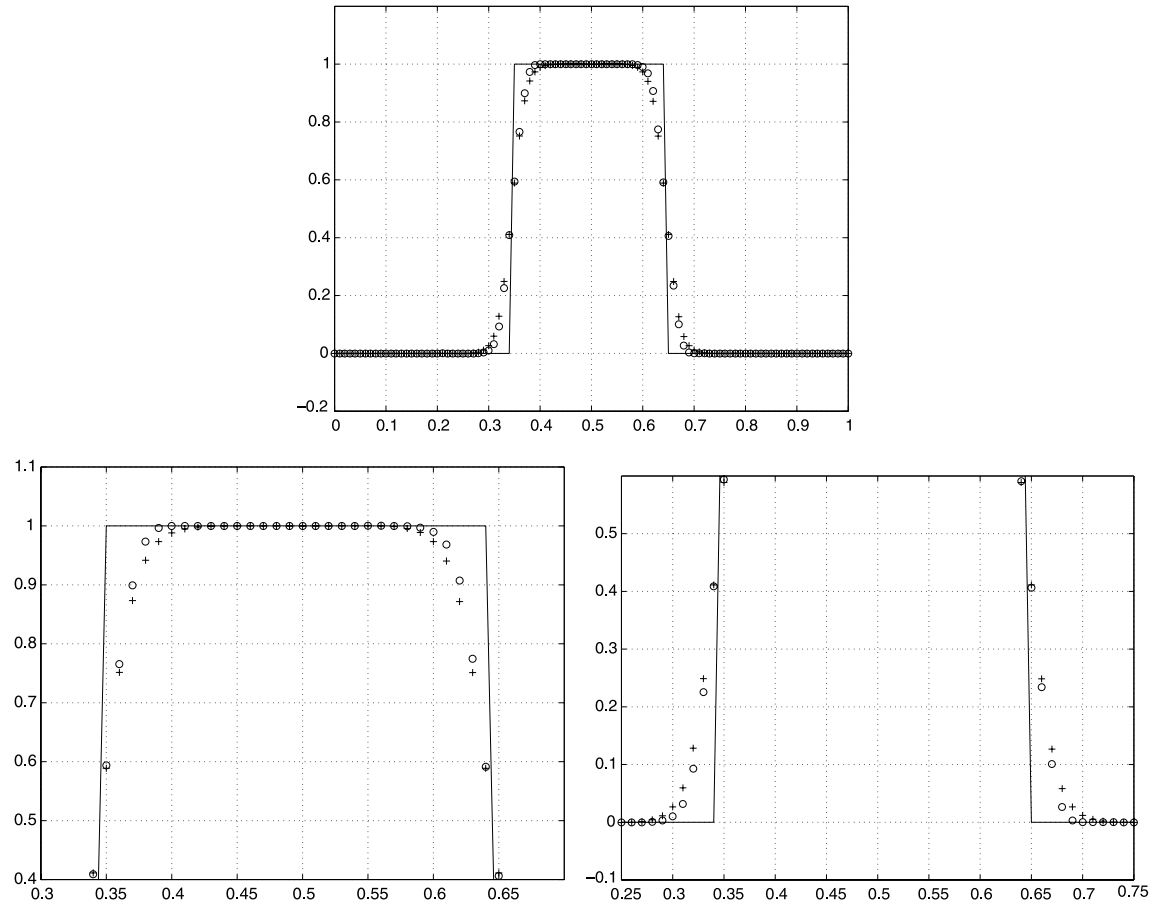

Fig. 6. WENO5 "+" and WPower-ENO5 "o".

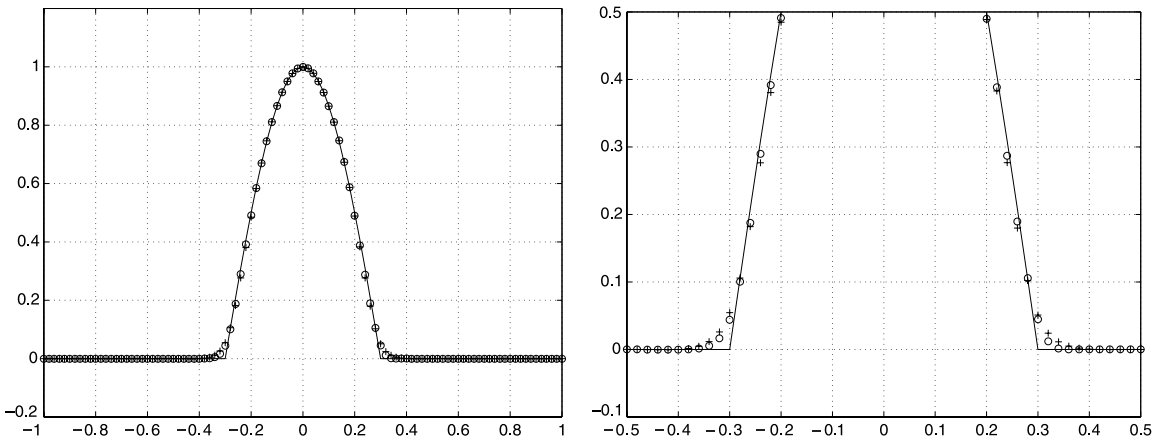

Fig. 7. WENO5 "+" and WPower-ENO5 "o".

$$\mathbf{u} = (\rho, M, E)^{\mathrm{T}}, \quad \mathbf{f}(\mathbf{u}) = v\mathbf{u} + (0, P, vP), \tag{61}$$

where ρ, v, $M = \rho v$, E and P are the density, velocity, moment, energy and pressure, respectively, and

$$E = \rho\epsilon + \frac{\rho v^2}{2}, \tag{62}$$

where ϵ is the specific internal energy and the system is closed with the equation of state (EOS), for ideal gases, which is written as $P = (\gamma - 1)\rho\epsilon$, being γ the adiabatic exponent. We have used the value $\gamma = 1.4$ in all our numerical tests.

We compare, for the Euler equations, the behavior of the fifth-order accurate reconstruction procedures under study WENO5 and WPower-ENO5. We will use Marquina's Flux Formula (MFF) by default [1] and, in some cases, Roe–Fix scheme (RF) [18].

The calculations were done using fifth-order accurate spatial reconstruction procedures applied to each characteristic flux obtained from physical fluxes by local linearizations computed at the interfaces following the so-called Shu–Osher "flux formulation" [18]. Indeed, if g is the characteristic flux, we reconstruct $\tilde{g}$ in cell $[x_{j-\frac{1}{2}}, x_{j+\frac{1}{2}}]$ such that $g(u(x_j)) = \frac{1}{h}\int_{x_{j-\frac{1}{2}}}^{x_{j+\frac{1}{2}}} \tilde{g}(\xi)\,\mathrm{d}\xi$ as explained in Section 2. Let us remark that

$$g(u(x))_{x_j} = \frac{\tilde{g}(x_{j+\frac{1}{2}}) - \tilde{g}(x_{j-\frac{1}{2}})}{h} \tag{63}$$

in this case. We compute $\tilde{g}$ by approximating the primitive function $G(x) = \int_{x_{j-\frac{1}{2}}}^{x} \tilde{g}(\xi)\,\mathrm{d}\xi$ using polynomial approximation/interpolation, and then, taking the derivative.

We use the third-order accurate Shu–Osher Runge–Kutta method [18] to evolve in time.

We consider the following Riemann problems:

5.2. Example 2: One-dimensional Riemann problems

$$u_0(x) = \begin{cases} (\rho_{\mathrm{L}}, v_{\mathrm{L}}, P_{\mathrm{L}}), & -5 \leqslant x < 0, \\ (\rho_{\mathrm{R}}, v_{\mathrm{R}}, P_{\mathrm{R}}), & 0 \leqslant x \leqslant 5. \end{cases}$$

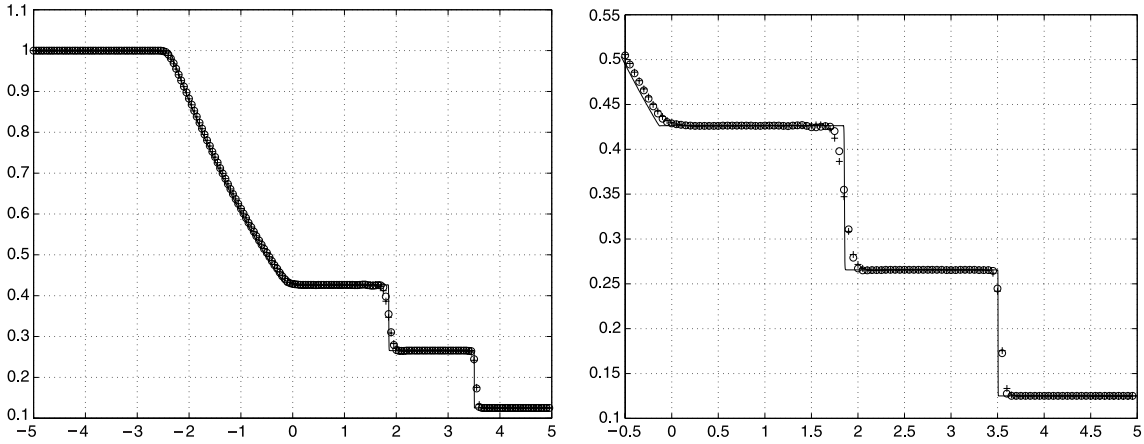

Fig. 8. WENO5-MFF "+" and WPower-ENO5-MFF "o".

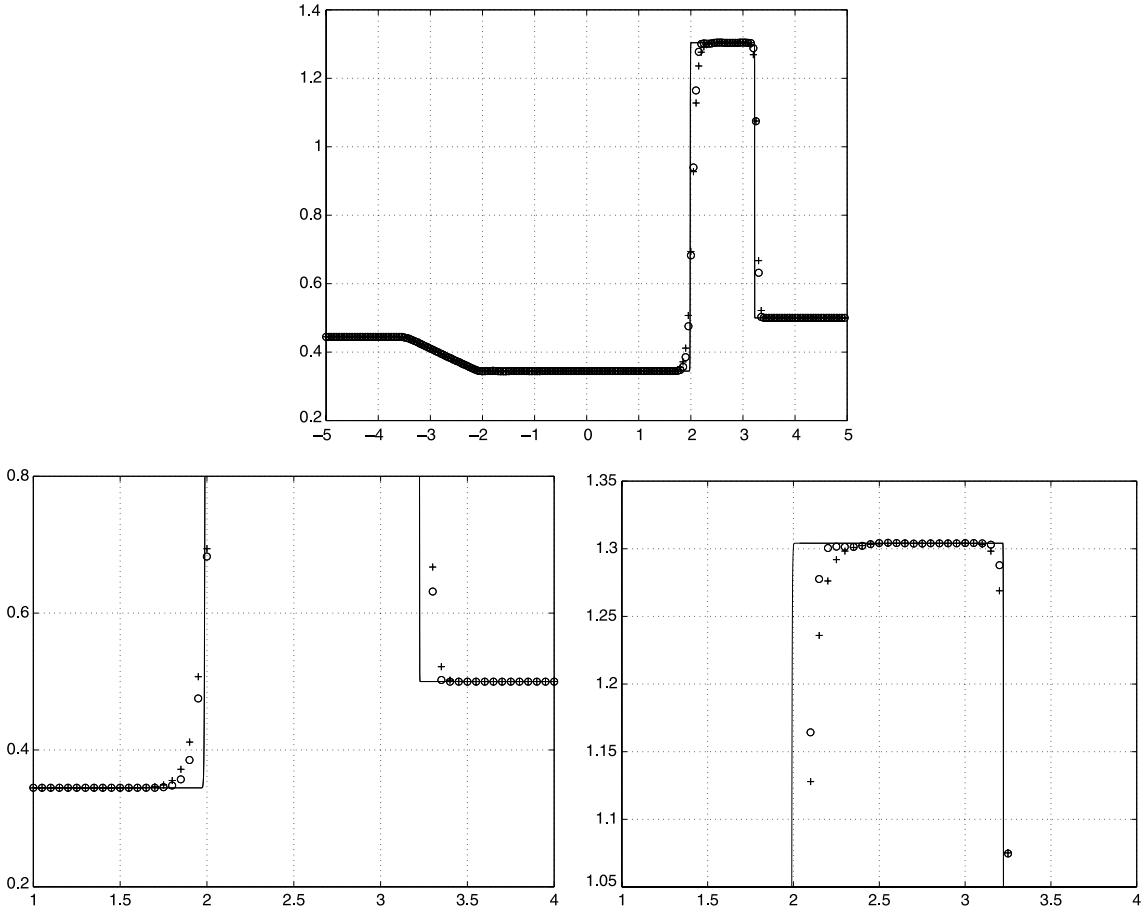

Fig. 9. WENO5-MFF "+" and WPower-ENO5-MFF "o".

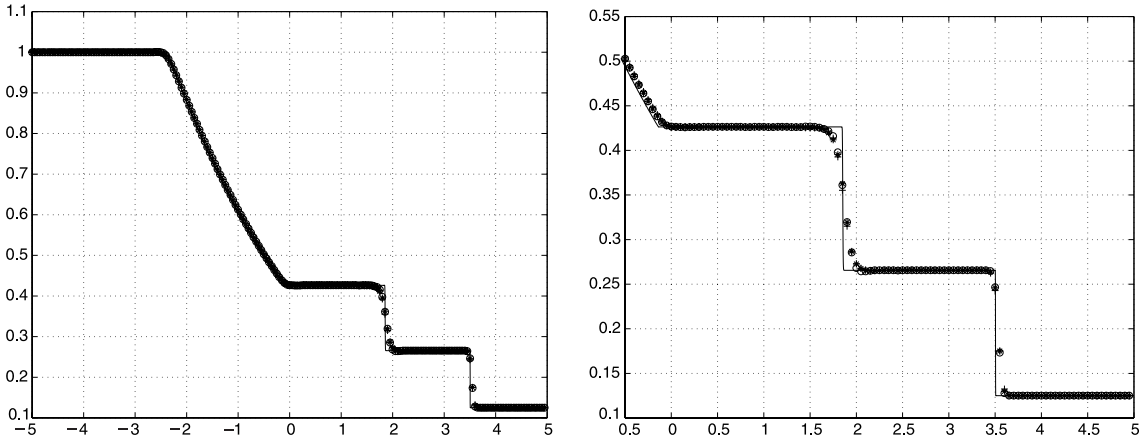

Fig. 10. WENO5-RF "+", WPower-ENO5-RF "o" and ENO5-RF "*".

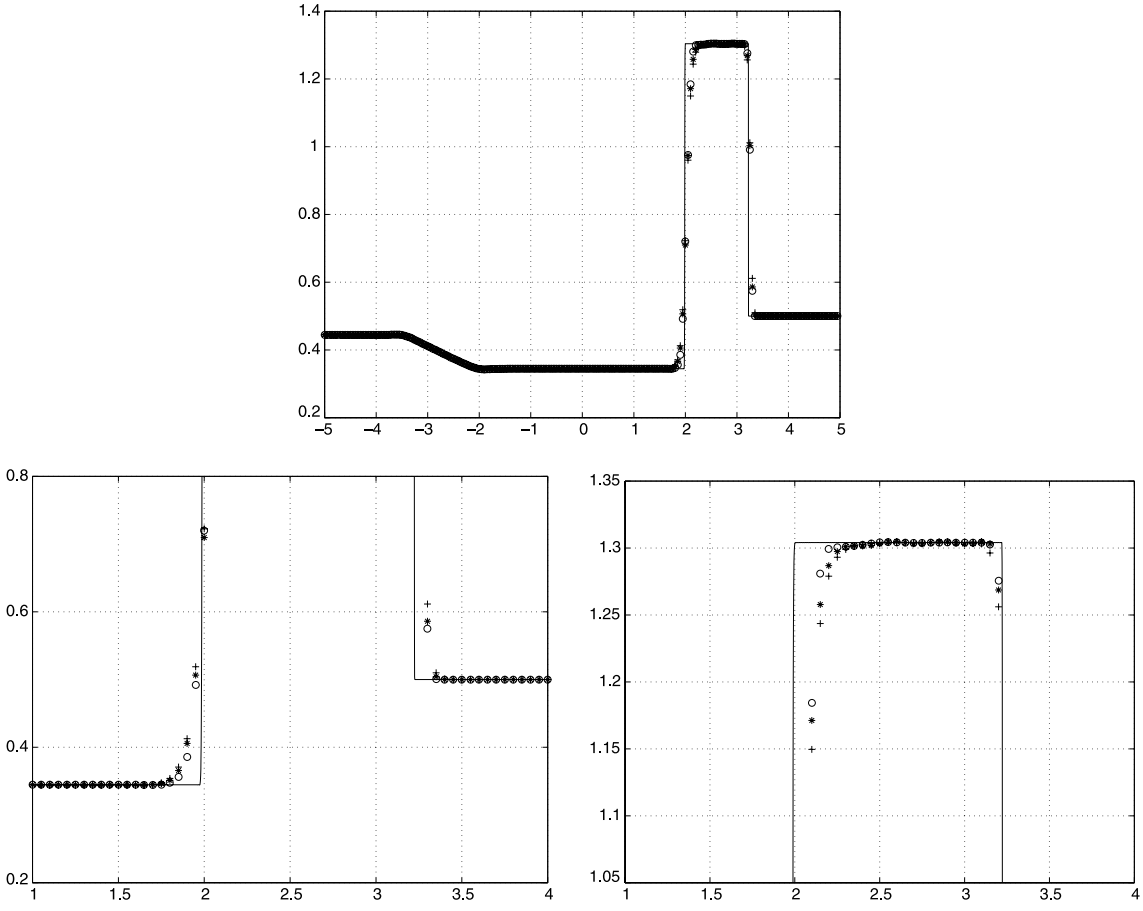

Fig. 11. WENO5-RF "+", WPower-ENO5-RF "o" and ENO5-RF "*".

5.2.1. The Sod's problem [19]

$$(\rho_L, v_L, P_L) = (1, 1, 1),$$

$$(\rho_R, v_R, P_R) = (0.125, 0, 0.1).$$

5.2.2. Lax's problem [6]

$$(\rho_L, v_L, P_L) = (0.445, 0.698, 3.528),$$

$$(\rho_R, v_R, P_R) = (0.5, 0, 0.571).$$

The computations for both cases were done using 200 equal spaced grid points with a constant ratio $\Delta t/h = 0.2$ until time 2 for the Sod's Tube and $\Delta t/h = 0.1$ until time 1.3 for the Lax's Tube. The solid lines represent the exact solution evaluated in 5000 points, see [16].

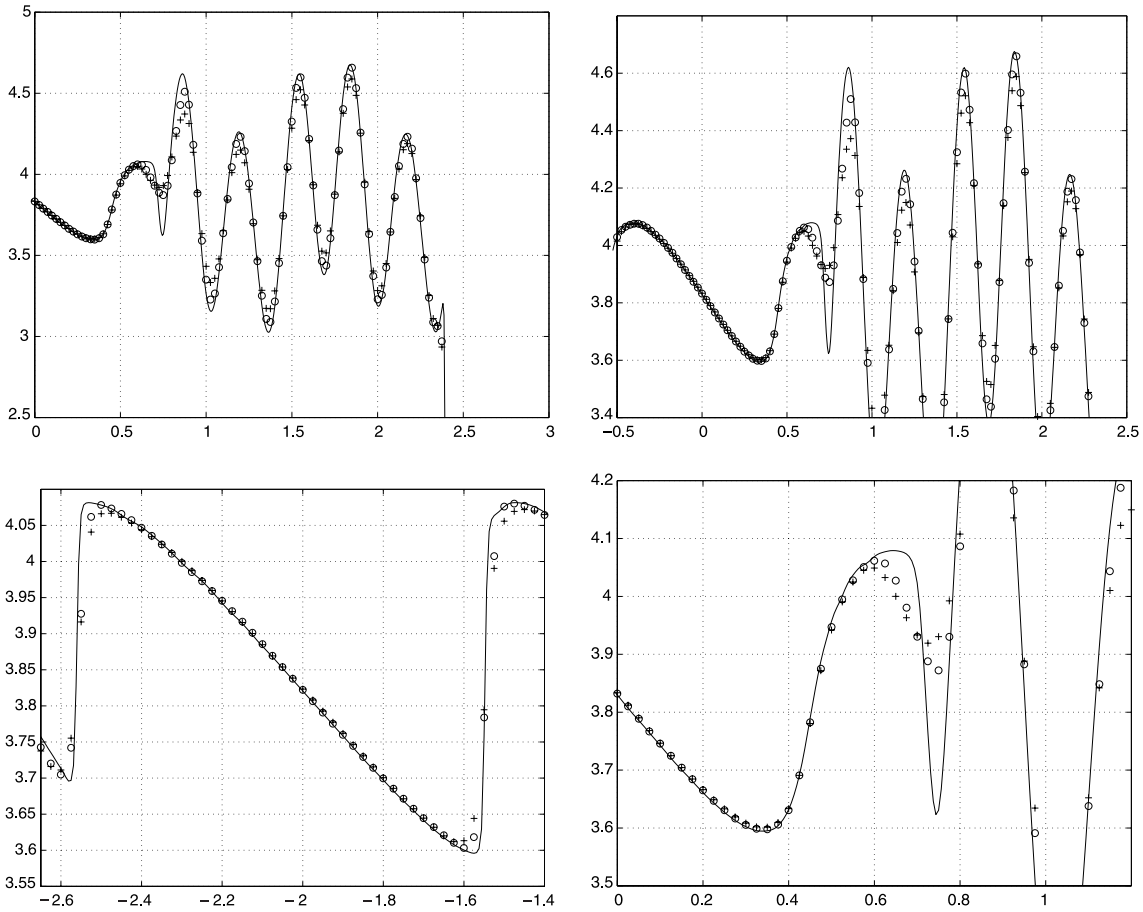

Fig. 12. zoomed regions of density profile, WENO5 "+", WPower-ENO5 and "o".

In Figs. 8 and 9, we display the numerical results of the density profile. The better behavior near discontinuities for our WPower-ENO5 method is more conspicuous for the Lax's Tube experiment (see zoomed regions at the bottom of Fig. 9).

In order to appreciate the behavior of the fifth-order Weighted ENO reconstruction methods with respect to the classical fifth-order ENO method, we have also computed both Riemann problems using Roe–Fix scheme. Indeed, we have implemented WENO5-RF, WPower-ENO5-RF and the classical ENO5-RF schemes using the Shu–Osher flux formulation.

In Figs. 10 and 11, we observe that WPower-ENO5-RF scheme resolves better the contact discontinuity than ENO5-RF and WENO5-RF schemes.

In what follows, we only use Marquina's Flux Formula as approximate Riemann solver.

5.3. Example 3: One-dimensional shock entropy wave interaction

Next, we consider a moving Mach 3 shock interacting with sine waves in density, used as a benchmark in Shu–Osher ([18], see also [12]).

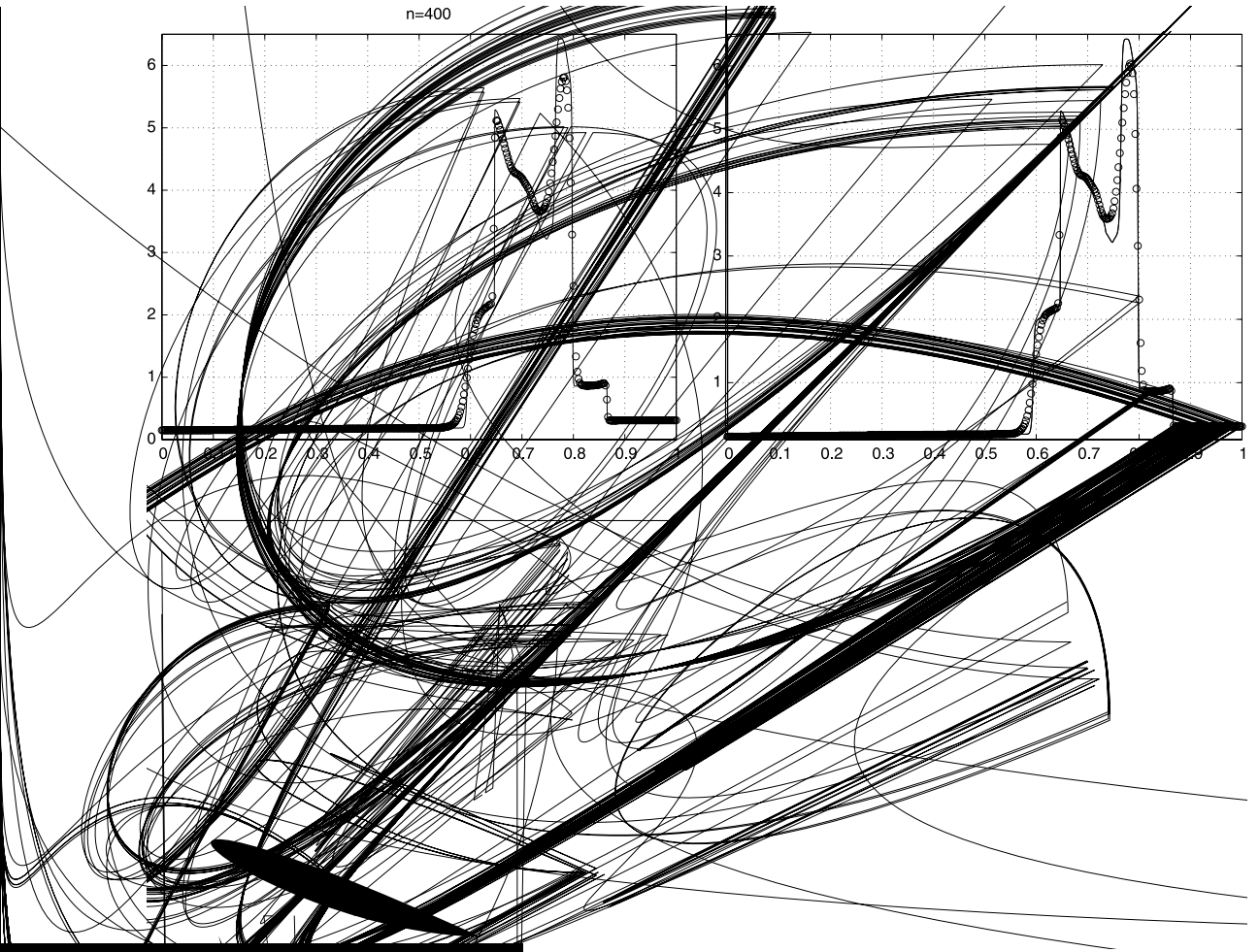

We consider the initial data:

$$u_0(x) = \begin{cases} (\rho_L, v_L, P_L), & -5 \leqslant x < -4, \\ (\rho_R, v_R, P_R), & -4 \leqslant x \leqslant 5 \end{cases}$$

$(\rho_L, v_L, P_L) = (3.85714, 2.62936, 10.33333)$ and $(\rho_R, v_R, P_R) = (1 + 0.2\sin(5x), 0, 1)$.

The numerical results of the density profile are displayed in Fig. 12. Solid line correspond to the numerical solution by WENO5 with 1600 points, that can be seen as the "exact" solution. We compute the numerical approximation for 400 points at time = 1.8 and $\Delta t/h = 0.1$ for WENO5 and WPower-ENO5, '+' and 'o' signs, respectively. We observe in Fig. 12 that fine structure in the density profile makes our WPower-ENO5 method to perform better than the WENO5 one. This feature is a consequence of the fact that the WPower-ENO5 method is more compressive (it produces more total variation in cell) than WENO5 method. On the other hand, we observe again a reduced smearing near shocks (see zoomed regions at the bottom of Fig. 12).

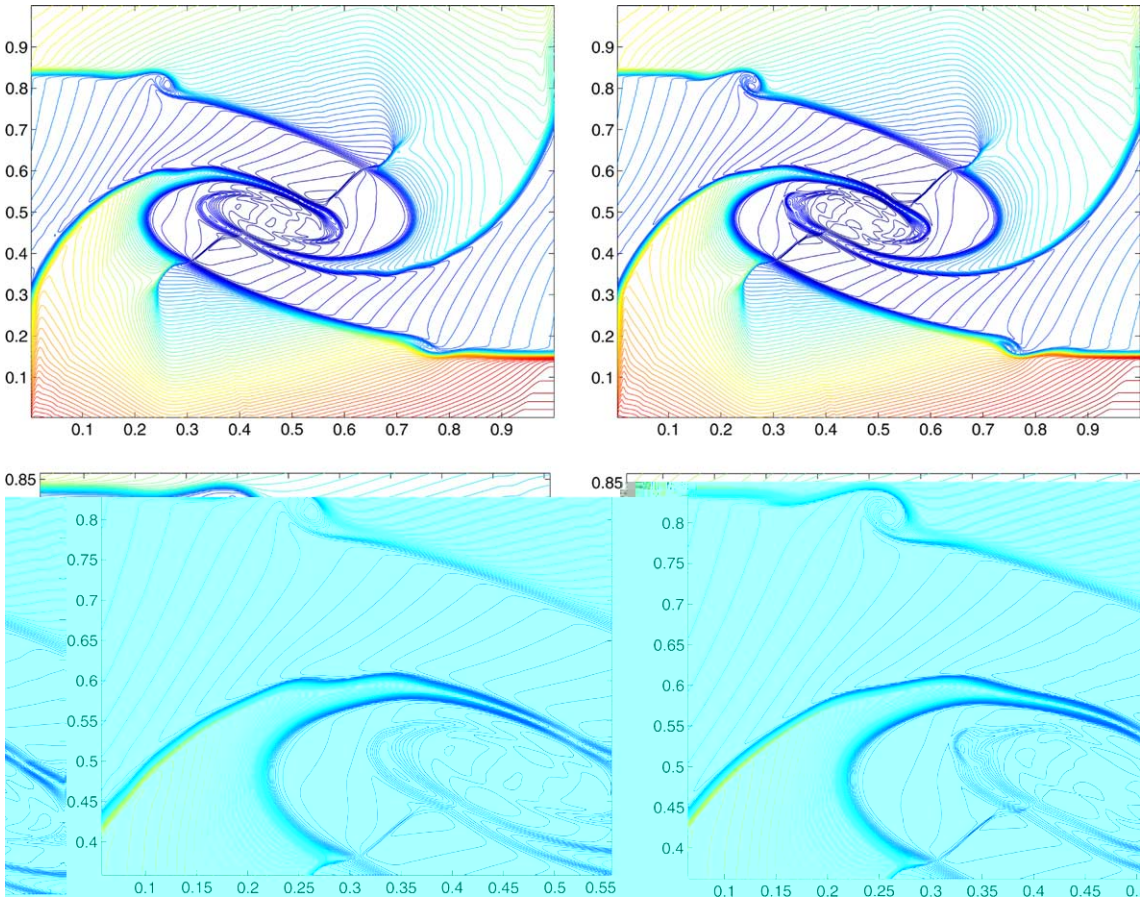

Fig. 14. WENO5 (left), WPower-ENO5 (right).

5.4. Example 4: Two interacting blast waves

This experiment was originally proposed as a benchmark by Woodward and Colella [20]

$$u_0(x) = \begin{cases} (\rho_L, v_L, P_L), & 0 \leqslant x < 0.1, \\ (\rho_M, v_M, P_M), & 0.1 \leqslant x < 0.9, \\ (\rho_R, v_R, P_R), & 0.9 \leqslant x \leqslant 1. \end{cases}$$

$(\rho_L, v_L, P_L) = (1, 0, 10^3)$, $(\rho_M, v_M, P_M) = (1, 0, 10^{-2})$ and $(\rho_R, v_R, P_R) = (1, 0, 10^2)$.

We display in Fig. 13 the density component computed with 400 and 800 grid points (top and bottom, respectively). We evolved until time 0.038 with $\Delta t/h = 0.01$ for WENO5 (left) and WPower-ENO5 (right).

We observe that the local extrema are better resolved for our WPower-ENO5 method. We did computations with different number of grid points and we observe good convergence rate to the "exact" solution (computed by WENO5 with 2000 points).

Finally, we will present two numerical experiments for the two-dimensional Euler equations for gas dynamics.

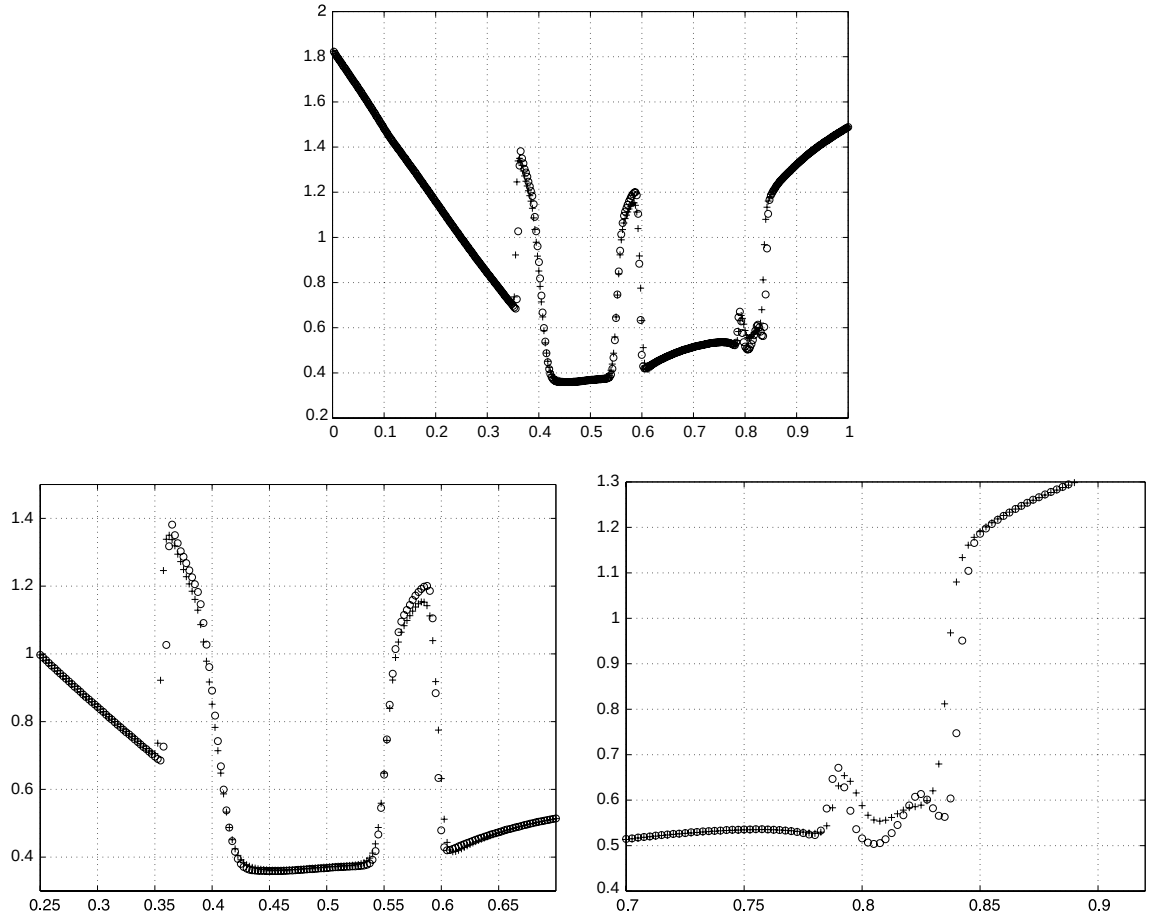

Fig. 15. Top, section of density profile at $x = 0.2575$. Bottom, zoomed regions of the x-section. WENO5 "+" and WPower-ENO5 "o".

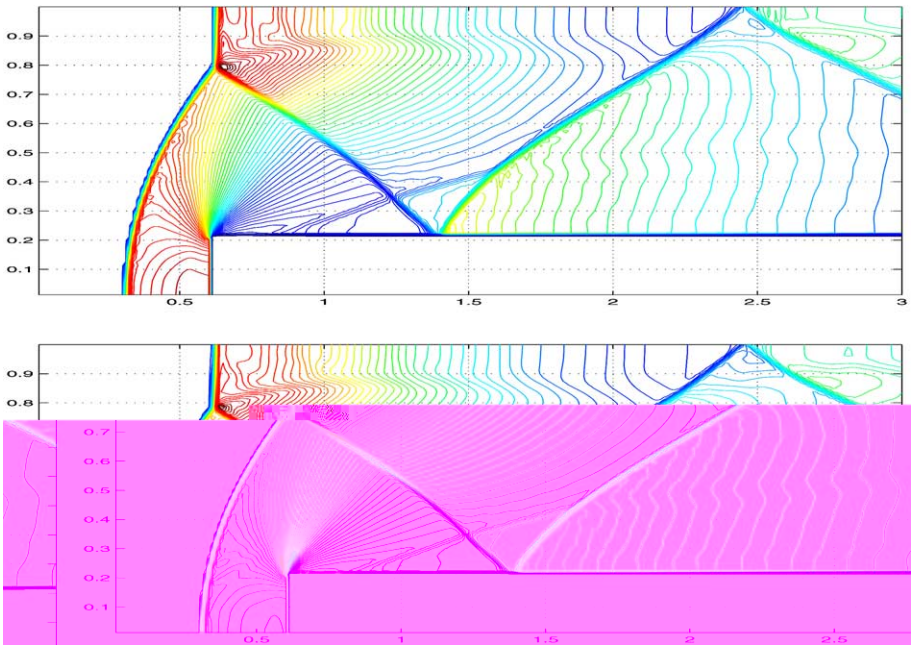

Fig. 16. Density profile, WENO5 (top) and WPower-ENO5 (bottom).

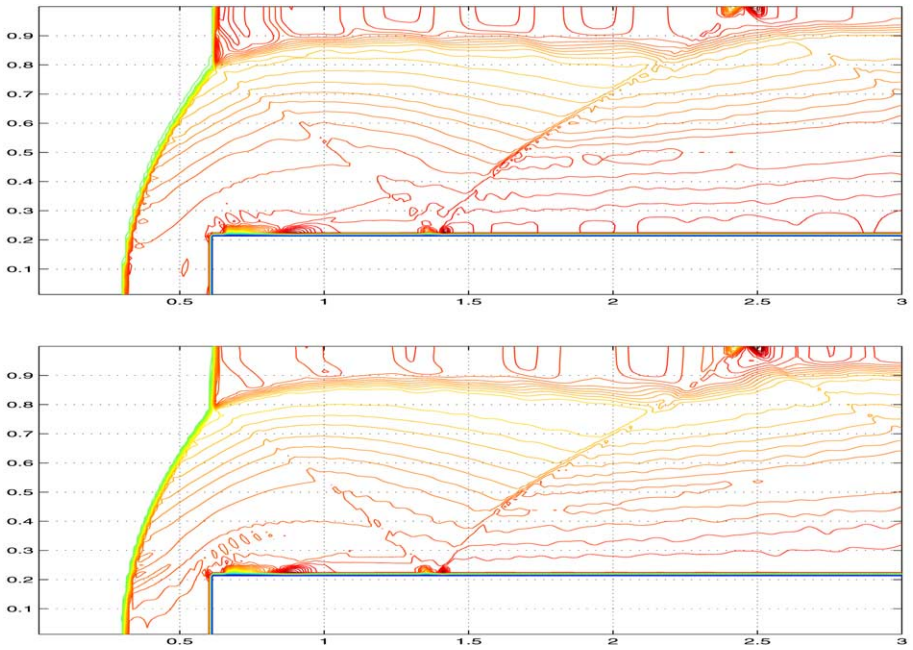

Fig. 17. Adiabatic constant P/ρ^{γ}, WENO5 (top) and WPower-ENO5 (bottom).

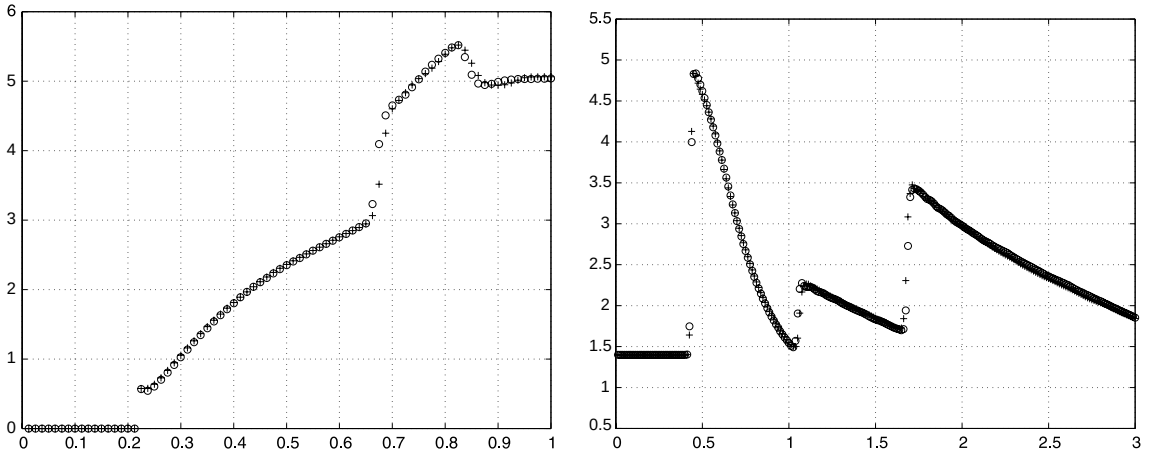

Fig. 18. Sections of density profile at $x = 0.8$ (left) and $y = 0.5$ (right), WENO5 '+' and WPower-ENO5 'o'.

5.5. Example 5: Two-dimensional Riemann problem

A two-dimensional Riemman problem consists in an initial data defined as constants states on each of the four quadrants. We consider the four contacts Riemann problem defined in [15] and we evolve this initial data until time 1.6, with a CFL factor of 0.8 for a grid of 400×400 points for WENO5 and WPower-ENO5 methods. We observe a better resolved vortex at the top for our WPower-ENO5 method at Fig. 14.

Also, we displayed at Fig. 15 a x-section, that traverses the vortex, showing the better resolution of the contact discontinuities of our WPower-ENO5 method versus WENO5 method (see the fine structure of the vortex region at the bottom of the figure).

5.6. Example 6: Mach 3 wind tunnel with a step

This test problem, introduced by Emery [2], has been carefully analyzed in [1,20]. The problem is initialized by a uniform Mach 3 flow in a tunnel containing a step. The tunnel is 1 length unit wide and 3 length units long. The step is 0.2 length units high and is located 0.6 units from the left-hand end of the tunnel.

Inflow boundary conditions are applied at the left-hand end and outflow boundary conditions are applied at the right-hand end of the computational domain. Reflective boundary conditions are applied along the walls of the tunnel. We use at the corner of the step the boundary entropy and enthalpy corrections discussed in detail in [1]. We use this example to test the robustness of our method in presence of reflective boundary conditions.

We evolve the initial data until time 4 for a grid of 240×80 grid points with a CFL factor of 0.8 . We display the contour lines of the density profiles in Fig. 16, and the adiabatic constant profiles in Fig. 17. We observe good resolution and location of the strong reflective waves appearing in this test and we have slightly better resolution at the contact line for our scheme.

In Fig. 18, we display sections of the density component. The left picture is the x-section at $x = 0.8$, where we observe better resolution of the weak contact for our WPower-ENO5 method.

6. Conclusions

We have introduced an extended class of limiters that includes the ENO limiters as particular case. These limiters are used to design total variation stable polynomial reconstructions when applied to second-order

differences. In this paper, we have proposed a new weighted ENO method, based on the extended limiters, that reaches optimal accuracy on smooth regions and improves the behavior of WENO methods near discontinuities. We presented several one- and two-dimensional numerical experiments for scalar and systems of conservation laws to show the evidence of the above features.

We remark that in numerical experiments where fine structures appear to be important (e.g., vortex regions), the Weighted Power ENO method shows substantial improvements in resolving fine scales, in spite of the improvements observed in standard numerical tests might seem to be minor.

References

[1] R. Donat, A. Marquina, Capturing shock reflections: an improved flux formula, J. Comput. Phys. 125 (1996) 42–58.
[2] A.F. Emery, J. Comput. Phys. 2 (1968) 306.
[3] A. Harten, High resolution schemes for hyperbolic conservation laws, J. Comput. Phys. 49 (1983) 357–393.
[4] A. Harten, B. Engquist, S. Osher, S. Chakravarthy, Uniformly high order accurate essentially non-oscillatory schemes III, J. Comput. Phys. 71 (2) (1987) 231–303.
[5] G.S. Jiang, C.W. Shu, Efficient Implementation of weighted ENO schemes, J. Comput. Phys. 126 (1996) 202–228.
[6] P.D. Lax, Weak solutions of nonlinear hyperbolic equations and their numerical computation, Commun. Pure Appl. Math. 7 (1954) 159–193.
[7] S. Li, L. Petzold, Moving mesh methods with upwinding schemes for time-dependent PDEs, J. Comput. Phys. 131 (1997) 368–377.
[8] R.J. LeVeque, Numerical Methods for Conservation Laws, Birkhauser Verlag, Zuerich, 1990.
[9] X-D. Liu, S. Osher, T. Chan, Weighted essentially non-oscillatory schemes, J. Comput. Phys. 115 (1994) 200–212.
[10] A. Marquina, Local piecewise hyperbolic reconstructions for nonlinear scalar conservation laws, SIAM J. Sci. Comput. 15 (1994) 892–915.
[11] A. Marquina, S. Serna, Afternotes on PHM: harmonic ENO methods, in: Proceedings of the Ninth International Conference on Hyperbolic Problems: Theory, Numerics, Applications, HYP2002, Caltech, Pasadena, CA, Springer, 2002.
[12] J. McKenzie, K. Westphal, Interaction of linear waves with oblique shock waves, Phys. Fluids 11 (1968) 2350–2362.
[13] S.J. Osher, S. Chakravarty, High resolution schemes and the entropy condition, SIAM J. Numer. Anal. 21 (1984) 955–984.
[14] A. Rogertson, E. Meiburg, A numerical study of the convergence of ENO schemes, J. Sci. Comput. 5 (1990) 151–167.
[15] C.W. Schulz-Rinne, J.P. Collins, H.M. Glaz, Numerical solution of the Riemann problem for two-dimensional gas dynamics, SIAM J. Sci. Comput. 14 (1993) 1394–1414.
[16] J. Smoller, Shock Waves and Reaction–Diffusion Equations, Springer Verlag, New York, 1983.
[17] C.W. Shu, Numerical experiments on the accuracy, J. Sci. Comput. 5 (1990) 127–150.
[18] C.W. Shu, S.J. Osher, Efficient implementation of essentially non-oscillatory shock capturing schemes II, J. Comput. Phys. 83 (1989) 32–78.
[19] G. Sod, A survey of several finite difference methods for systems of nonlinear hyperbolic conservation laws, J. Comput. Phys. 27 (1978) 1–31.
[20] P. Woodward, P. Colella, The numerical simulation of two-dimensional fluid flow with strong shocks, J. Comput. Phys. 54 (1984) 115–173.